UNIVERSITY OF SOUTHAMPTON

FEEG3003 INDIVIDUAL PROJECT

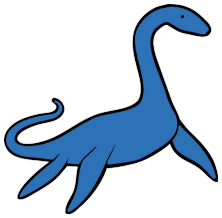

Aerodynamics of Tandem Flapping Wings

The application of flexible flippers in non-propeller based aquatic propulsion systems

Gavin Vales
gllv1g15@soton.ac.uk
 # 27733408

Supervisor: Professor Bharathram Ganapathisubramani

This report is submitted in partial fulfillment of the requirements for the Masters in Aeronautics & Astronautics Engineering degree program with Spacecraft Engineering Theme, Faculty of Engineering and the Environment, University of Southampton.

Word Count: 7271

Contents

Declaration of Academic Integrity

I, Gavin Vales, declare that this thesis and the work presented in it are my own and has been generated by me as the result of my own original research.

I confirm that:

1. This work was done wholly or mainly while in candidature for a degree at this University;
2. Where any part of this thesis has previously been submitted for any other qualification at this University or any other institution, this has been clearly stated;
3. Where I have consulted the published work of others, this is always clearly attributed;
4. Where I have quoted from the work of others, the source is always given. With the exception of such quotations, this thesis is entirely my own work;
5. I have acknowledged all main sources of help;
6. Where the thesis is based on work done by myself jointly with others, I have made clear exactly what was done by others and what I have contributed myself;
7. Either none of this work has been published before submission, or parts of this work have been published as:

    - Muscutt, Dyke, et al. (2017b)
    - Muscutt (2017)
    - Muscutt, G. Weymouth, et al. (2017a)

Acknowledgements

I would like to thank my supervisor for the mountain of insight provided in developing this thesis, and dealing with my procrastination.

Thanks to PhD candidate Nick Lagopoulos for the assisstance and valuable training he provided in the use of the flume tank apparatus.

And last but not least, many thanks to Dr. Muscutt who made this thesis posssible through all the work he did to build the flapping apparatus, set up the cRIO and for helping with the flipper manufacture.

Abstract

Biomimetics, or biomimicry as it is more commonly known, refers to engineering undertakings that aim to mimic the intricate and complex mechanisms that modern life has evolved via natural selection to overcome common engineering problems. For example, Hideo Shima's Kingfisher-inspired Japanese bullet train, which were used to increase the speed of the trains as well as reduce their noise production, and recent work on autonomous Micro Air Vehicles (MAVs) which mimic and utilise the flapping wing aerodynamics of flying insects, for high performance, low power flight.

Similarly, the Project Atlantis team at the University of Southampton are producing an Unmanned Underwater Vehicle (UUV) based on the flippers of the prehistoric plesiosaur, shown in Fig. 1.1.

The project described herein will take this one step further and investigate flexible flippers, something not yet investigated by Project Atlantis, by carrying out the same experiments as Project Atlantis, thus allowing for a direct comparison with rigid flippers, and a preliminary evaluation of the use of flexible flippers on the UUV.

1

Introduction

1.1 Project Overview

As already detailed, Luke Muscutt and the Project Atlantis team at the University of Southampton aim to produce an Unmanned Underwater Vehicle (UUV) whose propulsion system uses a tandem flapping wing arrangement, based on that of the prehistoric, aquatic, plesiosaur (Fig. 1.1). The project described in this report aims to contribute to Project Atlantis by investigating the effect of using flexible flippers in the tandem flipper arrangement, and in the process produce a flexible flipper that can be used on the Project Atlantis UUV.

The use of flexible flippers on the Atlantis UUV has not been investigated as yet since other flipper properties (flipper planform, maximum angle of attack, α_{max}, etc) obviously have greater effects on the performance characteristics of the flipper. Compared to these parameters, flexibility will likely only produce marked increases in tandem flipper performance. As a result, this report can also be seen as a preliminary insight into the use of flexible flippers, to make sure flexible flippers are viable.

Previous research on flexible wings, some carried out along with the work on MAVs, as well as independent work on single pairs of flexible flapping wings, showed significant increases in thrust production and propulsive efficiency (Section 1.3).

Having reviewed this past literature in the following sections, the objectives for this project will be derived in Section 1.4.

Figure 1.1: The Collard plesiosaur skeleton in Somerset County Museum, UK (Larkin et al., 2010) used by Muscutt et al to produce the flipper planform used in Muscutt, Dyke, et al. (2017b).

1.2 Tandem Flippers

Project Atlantis' work began with an explanation of how plesiosaurs used their similarly sized flippers (Fig. 1.1) as propulsors, and whether this arrangement had its advantages for locomotion,

all described in Muscutt's thesis (Muscutt, 2017). Previously, palaeontologists could only speculate what the extra pair of flippers was for, since the plesiosaur has no modern day analogues, ranging from speculations saying that the pairs of flippers flapped 180^o out of phase with each other (Frey et al., 1982), in phase with each other (Carpenter et al., 2010), or with a phase difference of 90^o or 270^o (Newman et al., 1967), to postulating that the hind flippers flapped only a little or not at all, simply being used for steering (Liu et al., 2015). As such, Muscuttt et al aimed to produce a detailed analysis of the plesiosaurs' propulsion, modelling this problem from an engineering perspective.

Similar work has been done, such as that by Usherwood et al. (2008) on changing the phase between each pair of dragonfly wings to maximise performance, and why there is an optimum phase for different regimes. Muscutt et al explore similar aspects of this topic, investigating various Strouhal No., St, and Reynold's No., Re (Muscutt, Dyke, et al. (2017b) and Muscutt, G. Weymouth, et al. (2017a)). The Strouhal No. is used to describe flows with oscillatory mechanisms, especially those flows involving aeroelastic mechanisms, and where vortices are shed, and important mechanism in flapping foil fluid mechanics.

Epps et al. (2016), working with Muscutt et al, asserts a relationship between the inter-foil spacing, s, & optimum phase, ϕ_{opt}, shown in Eq. 1.

$$\phi_{opt} = \phi_0 + \frac{2\pi}{U^*/U}\frac{s}{U\tau} \tag{1}$$

... where ϕ_0 is the phase that gives the highest efficiency at inter-foil spacing, $s = 0$, U^* the velocity of vortex advection, and τ the time period of one flapping cycle.

This equation was used to effectively reduce the number of degrees of freedom in the problem, allowing for simpler computational and experimental investigations.

The thrust generation in flapping wing aerodynamics is due to vortex generation on the front surface of the wing, then the shedding of these vortices at the peaks in the flapping cycle, resulting in a high speed jet downstream of the wing as the vortices advect. Therefore, in the tandem wing arrangement, how the aft wing interacts with the vortices from the fore wing is of interest.

Muscutt, G. Weymouth, et al. (2017a) carried out various computational analyses, using the Boundary Data Immersion Method (BDIM) developed by G. D. Weymouth et al. (2011), of s and ϕ to investigate this, finding that there *is* an optimum ϕ, where the aft foil can weave between the vortices shed from the fore foil, increasing the vorticity on the aft foil's front surface, and thus the strength of the vortices shed from the aft foil. These vortices mingle with those from the fore foil, creating a faster downstream jet than in the single foil case. For $St = 0.4$, this high performance case was found to be at $s = 2$ and $\phi = 7\pi/4$. In comparison, for the same St, at $\phi = 3\pi/4$, the aft foil encounters or is near to the fore foil's vortices, decreasing the vorticity on the aft foil's front

surface. The vortices shed from the aft foil are thus weaker, and the phase difference means that they don't mingle with the vortices from the fore foil. So, the downstream jet in this regime is weaker, and the flippers produce less total thrust.

Interesting observations can *also* be made from the contour plots produced in Muscutt, G. Weymouth, et al. (2017a) (using 80 tandem foil simulations), illustrating thrust and efficiency variation for different s and ϕ combinations at $St = 0.2, 0.3, 0.4$ & 0.5. Fig. 1.2 and Fig. 1.3 are examples of these pots, at the maximum and minimum St regimes investigated. In Fig. 1.3, it can be seen that the minimum value on the contour plots decreased with St, suggesting stronger detrimental flow mechanisms with increasing f.

Not seen in the contour plots is how the maximum value on the plots is related to the efficiency of the fore foil, since if the fore foil is operating at maximum efficiency, then lower thrust augmentation can be observed.

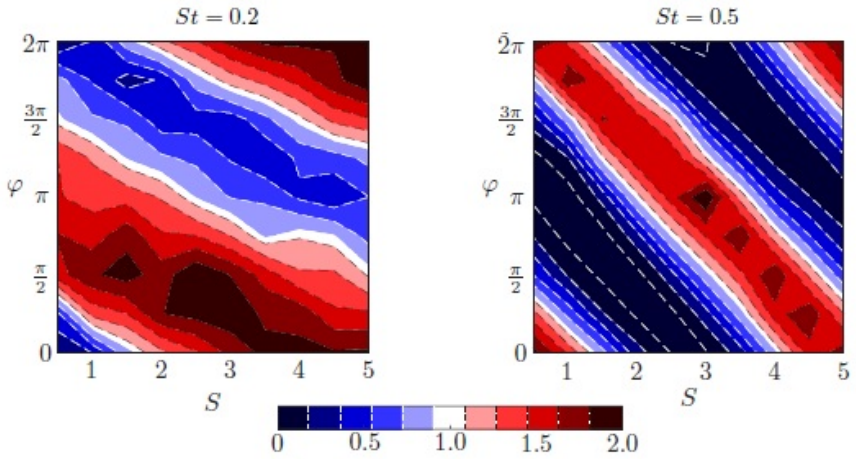

Figure 1.2: Contour plots of the mean measured thrust coefficient of the aft foil, at $St = 0.2, 0.5$ compared to the isolated foil thrust coefficient $C^*_{T,h,m}$ (Muscutt, G. Weymouth, et al., 2017a)

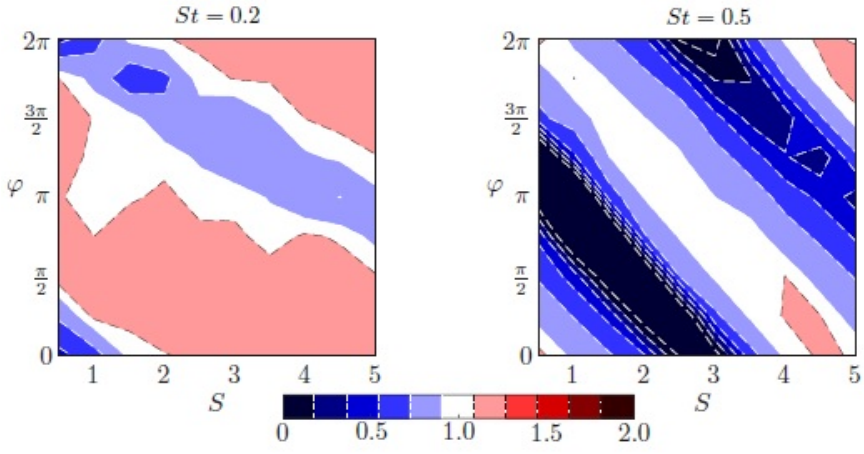

Figure 1.3: Contour plots of the mean measured efficiency of the aft foil, at $St = 0.2, 0.5$ compared to the isolated foil efficiency $\eta^*_{h,m}$ (Muscutt, G. Weymouth, et al., 2017a)

Experimental confirmation of the findings in Muscutt, G. Weymouth, et al. (2017a) is found in Muscutt, Dyke, et al. (2017b).

Using a water flume and two flippers, arranged one in front of the other, attached to a mechanism to oscillate them in heave/pitch, Muscutt, Dyke, et al. (2017b) confirmed the performance-phase angle relationship, at different values of Strouhal number, St, and α_{max}. Most data was collected at $U = 0.22ms^{-1}$, and some at $U = 0.44ms^{-1}$.

At the optimum phase, the tandem flipper arrangement produced about 60% more thrust, and 40% greater efficiency than an isolated single flipper. Further, ϕ_{opt} was different for different St, confirming Eq. 1. At high St, $\phi_{opt} \approx 270^o$ (hind flipper lags), and at low St, $\phi_{opt} \approx 45^o$ (hind flipper leads). Also, at lower St (≈ 0.18), the efficiency was found to be greatest, and at higher St (≈ 0.36), the thrust coefficient was greatest (i.e. C_T increased with St, while η decreased with increasing st). So the general trends in Fig. 1.2 & Fig. 1.3 hold for real flows.

Thus, Muscutt et al conclude that Plesiosaurs employed different flipper motions for different swimming conditions, using low St for high efficiency *cruising* gaits, and high St for high thrust *sprint* gaits.

Flow visualisation dyes were used and confirm the mechanisms driving the performance augmentation in a flapping tandem wing arrangement, described in Muscutt, G. Weymouth, et al. (2017a).

This experimental investigation also shows that increasing the flipper spacing, s, with constant U, has a detrimental effect on the performance augmentation arising from the aft flipper since the vortices shed from the fore flipper will advect a greater distance before reaching the aft flipper, losing more energy due to viscous effects. However, when s is roughly 7 & 3 chord lengths, the performance augmentation is very similar, leading to the final conclusion that most plesiosaurs would have experienced benefits from their unique flipper arrangement.

With the confirmations, produced in Muscutt's experimental work, of the computational methods used in Muscutt, G. Weymouth, et al. (2017a), it can be seen that the work of Muscutt et al can be regarded as reliable. Even with the relatively simple experimental simulation in Muscutt, Dyke, et al. (2017b), valuable insights were provided into plesiosaur locomotion, and the viability of the use of tandem flippers as propulsors has been shown. More detailed investigations will need to be carried out to analyse more complex regimes (yaw and roll for example) and more varied flipper properties (planform and flexibility).

Epps et al. (2016) also computationally investigated how the introduction of the hind flipper pair affected the instantaneous thrust and side-force variations acting on the whole UUV. Epps found that for specific values of ϕ, those variations could be minimised: the thrust variation being minimised when $\phi = \pi$ 2, and the side-force variation minimised when $\phi = \pi$. A trade-off can be found at

$\phi = 3\pi/4$.

These insights make tandem wing propulsion systems extremely desirable.

1.3 Flexible Wings

Shusheng et al. (2012) explores how span-wise flexibility affects a flapping wing's performance in low Reynold's number flow ($10000 < Re < 20000$), and St between 0.1 & 1.0. St in this investigation is calculated using the amplitude of the wing's midspan as the characteristic length, to negate detrimental phase lag effects that may occur at the wing tips of highly flexible wings. The characteristic length used in calculating Re is the effective chord length of the wings. Span-wise flexibility was changed by varying the thickness of a fin ray running along the wing span, producing four wings of different flexibility, defined by the ratio of their tip deflection to their span length, α_{tip}/l_{span}, when a mass of 0.1 kg is applied to the tip. This assembly ensures that chord-wise flexibility isn't changed.

With this set up, Shusheng and Yueri found that increasing span-wise flexibility caused the wing to produce negative thrust for a greater proportion of the flapping cycle. Analogous to the findings of Muscutt et al, the optimum span-wise flexibility was found to change with Strouhal number, with the most flexible wing producing the greatest average thrust at lower St, up to about $St = 0.5$, above which the second most flexible wing produced the most average thrust. Wu et al. (2011) reports similar findings. This is due to the high phase lags that a flexible wing would experience at comparatively high f, causing detrimental wing tip effects. Generally, the average thrust was found to increase with both St and Re.

The average thrust, $\bar{F}/N$ was calculated using the thrust profile from 3 flapping cycles out of 5, omitting the first and last cycles to reduce any errors from them.

Shusheng et al. (2012) also found that power input coefficient, C_P, increased with spanwise rigidity. Conceptually, this can be expected, since a more rigid wing would have greater internal bending moments, and so require more work to displace the fluid flow. A wing that can undergo aeroelastic deformation would have lower internal bending moments, so needs less work to displace the flow. C_P was calculated using the voltage & current of the motor driving the flapping oscillations, and the theoretical efficiency of the driving system (which does mean that the actual power input was greater).

Shusheng et al. (2012) also shows that there is an optimum propulsive efficiency for each of the flippers. The two most flexible flippers had maximum efficiencies occurring in the range $0.2 < St < 0.4$, with very slight decreasing trends above $St = 0.4$. The two most rigid flippers saw sharp increases in efficiency to the maximum in the same St range, and then sharp decreases from the maximum. Aquatic animals that use flapping wing propulsion operate in these St ranges (Taylor et al., 2003).

Maximum efficiency increased with Re, as well as spanwise flexibility. The most flexible flipper (with $\alpha_{tip}/l_{span} = 0.485$) had the highest efficiency of 23.8 % at $Re = 20000$, due to their low power consumption, and relatively high thrust production (Shusheng et al. (2012) defines efficiency as $\eta = C_T/C_P$, the ratio between the thrust coefficient and power coefficient).

Heathcote et al. (2008) investigated spanwise flexibility as well, seeing similar benefits in the same St range. Using PIV, the reported initial C_T increase with flexibility was due to an increase in the effective heave amplitude. Excessive flexibility meant too much phase lag caused the formation of two vortices in an opposite sense to each other at the root and tip, leading to weak and fragmented vorticity patterns.

Barannyk et al. (2012) investigated chord-wise flexibility of flat plates, after Young et al. (2009) postulated that wing deformation is necessary for efficient momentum transfer to the wake, seeing similar increases of C_T with St, from a critical St of 0.16, as the wake transitioned from producing a net momentum deficit, to producing a net momentum excess, as well as similar η-flexibility profiles in the already discussed St range.

St_{crit} wasn't the same for all flexibilities. The most flexible plate had the lowest St_{crit}. Thus, St_{crit} depends on the heave amplitude to chord ratio, and α_{max}, not just the chord-wise flexibility.

Katz et al. (1978) explains that increase of η with flexibility is cause by increased chord-wise plate curvature, causing decreased lift force amplitude, but pulling the direction of the lift vector towards the plate advance.

Barannyk et al. (2012) goes further in the definition of the η-St profiles: they begin with a monotonic increase to η_{max} at the optimum St, then an asymptotic decrease to $\eta = 18\%$ for all flexibilities. Thus, the final conclusion can be made that chord-wise flexibility is good for small heave amplitudes.

1.4 Aims & Objectives

With the above literature in consideration, this IP will investigate the span-wise flexibility of tandem flexible flippers.

It would be interesting to quantify the observed performance augmentations, if any, for tandem flexible flippers and compare these to their rigid counterparts.

Thus, if the final experimental results show that the flexible flippers outperform their rigid counterparts, their viability for use on the Atlantis UUV can be assessed, and a rudimentary set of parameters for flexible flippers will be produced to run more realistic investigations, with flexible flippers being attached to the Project Atlantis UUV.

In addition, the behaviour of the flexibility mechanisms described in Section 1.3 will also be qualified, to help determine further investigations of different regimes, time-permitting.

2

The Flippers

2.1 Manufacture

The flippers were 3D printed using a FormLabs Form 2 3D printer, using Formlabs' proprietary flexible photo-polymer resin (FLFLGR02). Flipper flexibility was changed by incorporating an endoskeleton into the flipper CAD models, so that flexibility could be varied by changing the material properties of the endoskeleton, similar to the flexible wings in Shusheng et al. (2012). This method of changing the flipper flexibility was chosen to allow conservative use of manufacturing materials, mostly due to the high cost of the photo-polymer resin (roughly 20 GBP per print).

3 materials were chosen for the endoskeleton: 2mm thick CK75 hardened spring steel, 3mm acrylic perspex, and 3mm Plastazote LD33 foam (similar to that used in yoga mats).

Fig. 2.1 and Fig. 2.2 show how the flippers are designed and assembled. Fig. 2.1 shows the endoskeleton (3), the CK75 steel in these images, is epoxy glued to a laser-cut acrylic perspex aerofoil section (4). The endoskeleton can then be inserted in the flipper (1), with the attachement rod (2) being threaded through a hole in the perspex aerofoil. Once the endoskeleton is fully inserted in the flipper, a Cotter pin (5) is inserted through a hole (6).

Figure 2.1: Images of the assembly used to stop the endoskeleton from slipping out of the flipper when the flipper is deflected.

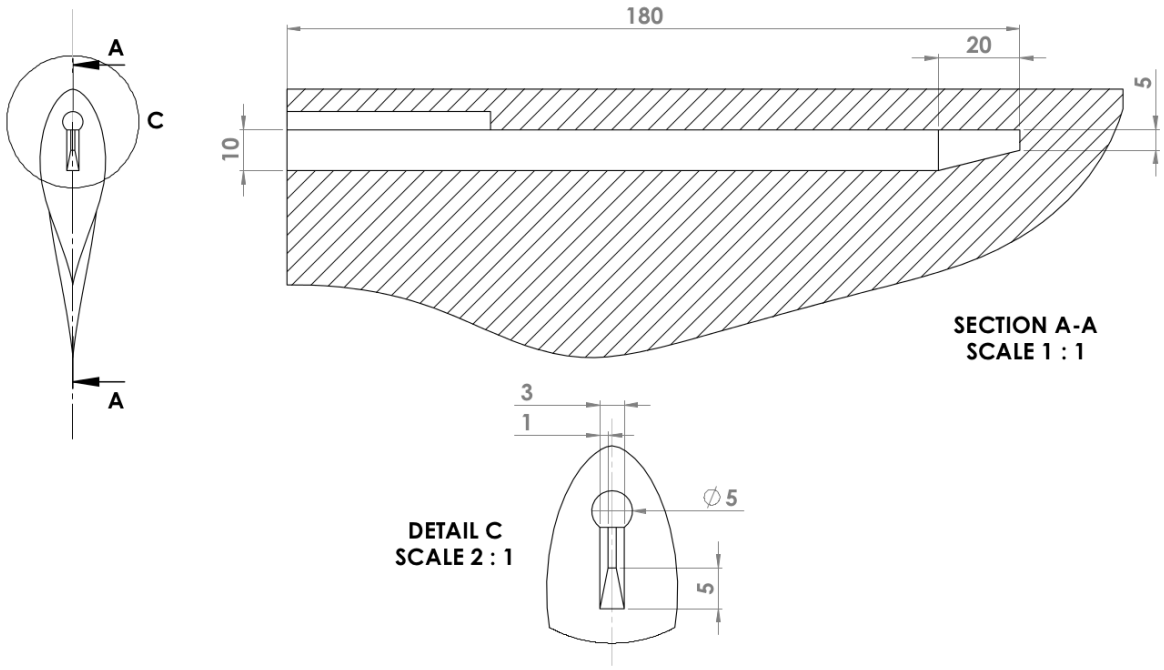

Figure 2.2: Drawing of the flipper with cut outs for the endoskeleton and attachment rod.

The endoskeleton dimensions (length, l = 180mm, width, w = 9mm and thickness, t = 2mm, 3mm) were chosen to allow the endoskeleton to be thick enough to produce noticeable changes in flipper flexibility, while still being thin enough so the walls of the flipper near the endoskeleton are not so thin that there is danger of the walls tearing when the flipper is being deflected (due to the internal shear forces and bending moments of the endoskeleton).

These constraints also drove the width of the endoskeleton, as well as its length, which is why the endoskeleton doesn't span the entire flipper, and why it tapers in its width and length directions towards the tip of the flipper (to ensure that there is at least a 1mm clearance between the endoskeleton and the outer surface of the flipper).

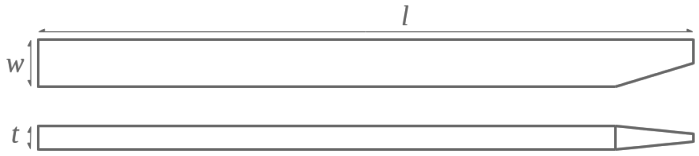

Figure 2.3: General schematic of endoskeleton.

Another driver for decreasing the endoskeleton width was that only span-wise flexibility was to be investigated, and thus chord-wise flexibility couldn't vary greatly between each flipper flexibility.

However, even with these precautions, the tearing risk was still present. Thus, a tougher plastic skin, similar to that used for plastic bags, was glued to the tip using a flexible glue, to reduce the risk of the flipper tearing.

With interchangeable endoskeletons, only 2 flippers would need to be printed. Another pair of flippers were printed, this time the only cut out sections being for the 5mm rod used to attach the

flippers to the flume tank carriage system, producing 1 more flexible flipper configuration that can be investigated.

Tab. 2.1 lists the finalized flipper configurations used for the flume-tank experiments. The AR4S flippers are the fully rigid flippers, 3D printed by Dr. Muscutt.

Flipper	Main Material	Endoskeleton Material
FL1	Flexible Resin	Foam
FL2	Flexible Resin	Flexible Resin
FL3	Flexible Resin	Perspex
FL4	Flexible Resin	Steel
AR4S	PLA	N/A

Table 2.1: Summary of materials used for each flipper configuration.

2.2 Defining Flipper Flexibility

To characterise the flexibility of the flippers shown in Tab. 2.1, the product of their Moment of Inertia, I, about their pitch axis and along their axis of deflection, and their effective Young's Modulus, E_{eff}, had to be found.

The flippers were first modelled in CAD using Dassault Systèmes' SolidWorks. Each part of the flipper was modelled, including the attachment rod and endoskeleton, and then assembled together. The flipper model (the same model used to create the drawing in Fig. 2.2) was provided by Dr. Muscutt. SolidWorks was used as it could easily find each flipper's moment of inertia, using its ability to evaluate a structure's mass properties in a given coordinate system. Fig. 2.4 illustrates this coordinate system.

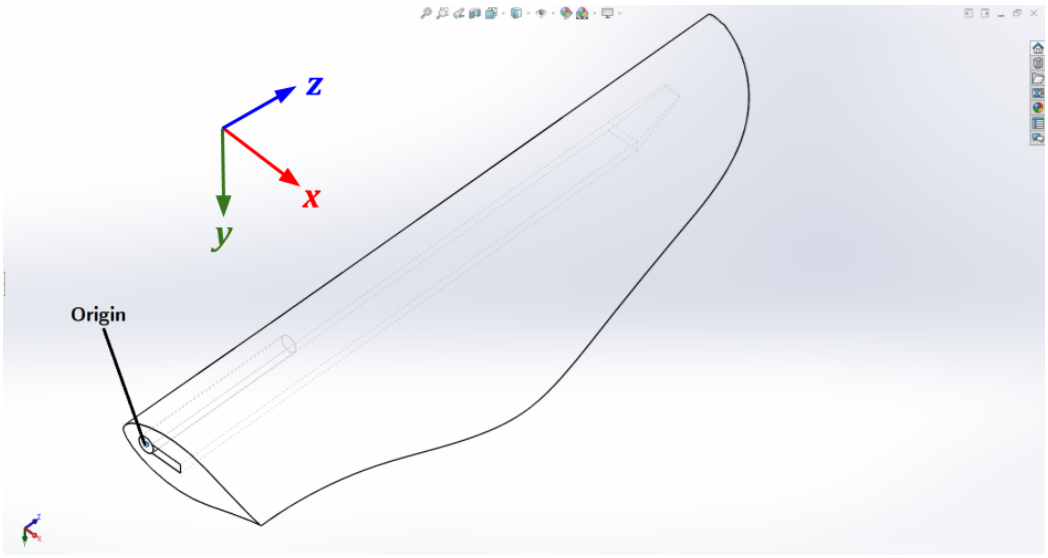

Figure 2.4: The coordinate system used by Solidworks to calculate the moment of inertia of each flipper assembly.

Using this coordinate system, it can be seen that the relevant element of the inertia matrix that will need to be extracted is the I_{xx} element.

E_{eff} for each flipper assembly was found by summing the values of E for each individual component, weighted by volume, giving

$$E_{eff} = \sum_{i=1}^{n} E_i V_i \tag{2}$$

where E_i is the Young's Modulus of each individual flipper component, and V_i the volume fraction of each flipper component.

Various online resources were used to collate the relevant values of E for each flipper component.

The perspex required for the endoskeleton was purchased from Plastic Online, which provides datasheets for its products on its website (Online, n.d.). Thus, E for cast acrylic perspex is found to be 3210 MPa, from the relevant datasheet (Ltd., n.d.).

Young's modulus data for the CK75 steel had to be obtained directly from the seller via a query, and is quoted to be 206 GPa.

The attachment rod was made from stainless steel, which has $E = 180$ GPa, as listed by Toolbox (n.d.).

Innofil3D has complete and informative datasheets for the Professional Series 3D printing filament used in the AR4S flipper, found at Innofil3D (n.d.). The value of E used for this flipper was 2635.5 MPa, an average of the maximum and minimum values quoted in the datasheet.

Since it's difficult to characterise the Young's modulus of elastic polymers, Formlabs does not have any technical data on this in its datasheets for the FLGR02 flexible resin (Formlabs, n.d.). However, Formlabs does advertise this resin as having an 80A hardness (on the Shore-A hardness durometer), so Eq. 3, from Gent (1958), was employed to convert Shore-A hardness to Young's modulus. This gives $E = 9.35$ MPa (2 decimal places).

$$E = \frac{0.0981(56 + 7.62336S}{0.137505(254 - 2.54S)} \tag{3}$$

Appendix A shows the python code used to calculate EI from these values, and its results tabulated in Tab. 2.2.

EI is converted to a non-dimensional form, $(EI)^*$, using Eq. 4, where $2l$ is the same characteristic length used to determine the Strouhal No. of the of the motion, m the mass of the flipper assembly, and q_∞ the dynamic pressure of the flow around the flipper.

$$(EI)^* = \frac{EI}{q_\infty m(2l)^2} \tag{4}$$

Flipper	EI $[kg^2ms^{-2}]$	$(EI)^*_{case123}$	$(EI)^*_{case4}$
FL1	1383443	138200102	23801513
FL2	1539904	142664340	24570366
FL3	1652124	153943120	26512854
FL4	9586271	706554918	121686421
AR4S	3291157	277553182	47801597

Table 2.2: Table showing EI, $(EI)^*$ values for each flipper flexibility.

Flipper	**Rank**	$(EI)^*_{norm}$
FL1	R1	0.498
FL2	R2	0.514
FL3	R3	0.555
FL4	R5	2.546
AR4S	R4	1.000

Table 2.3: Table ranking each flipper configuration based on their normalised $(EI)^*$ values.

As expected, increasing $(EI)^*$ corresponds to increasing spanwise rigidity. To slightly simplify further analysis, the flippers have been ranked according to their normalised $(EI)^*$ values in Tab. 2.3, and will be referenced with respect to these rankings for the remainder of this report. $(EI)^*_{norm}$ is independent of the flow regime, so can be used for all flume experiments carried out (see Section 3.3).

$$(EI)^*_{norm} = \frac{(EI)^*}{(EI)^*_{AR4S}}$$

3

Experimental Set-up

3.1 Apparatus

Fig. 3.1 and Fig. 3.2 show the apparatus created by Luke Muscutt used to heave and pitch the flippers. The axes superimposed on both figures are those used by the load cells (4) on the hind flipper. All data used in this report are taken from these load cells.

The flippers are attached, at (1), to the pitching stepper motors (2). These motors are attached to linear rails (3) allowing another pair of stepper motors to heave the flippers as well.

The flipper motion is controlled via a National Instruments cRIO that contains LabView VIs, also created by Luke Muscutt, which both acquire data from the load cells on the hind flipper, and produce the necessary auxiliary data for setting up the data processing phase of the experiments, such as producing calibration matrices for the load cells (4) on the hind flipper (H), taking the initial zero data (when the flume is off), as well as being able to zero the flippers and heave or pitch them in both linear or oscillatory motion.

3.2 Single Case

The method for acquiring the data for a full singular case is described in the following. During a single case, these variables are kept constant: flipper spacing, s, flapping frequency, f, flapping amplitude, l, flipper aspect ratio, AR, and flow velocity, U_∞. This leaves only the phase, ϕ, that can be changed.

Data for a full singular case is acquired by first

- Attaching the flippers to the flapping apparatus.
- Turning on the stepper motors (which heave and pitch the flippers) and the cRIO (which controls the stepper motors and acquires data from the load cells).

The flippers are then centred, using the cRIO, with respect to their heave and pitch axes, so that they have an angle of attack, $\alpha = 0$, and are aligned on the centreline shown in Fig. 3.2, before the flapping motion has begun.

1. While the flume is off and the flippers are stationary, two sets of the initial zero data can be acquired.
2. Once the initial zero data has been taken, the main data set can be acquired, after the flume tank is turned on. The flippers are flapped in heave, with amplitude l, and in pitch, with amplitude 45^o, at flapping frequency, f, for 100 flaps, while the cRIO records the data from the load cells during this motion.
3. The flippers are centred once again at the end of the flapping motion.

4. Steps 2 & 3 are carried out for each of 16 phase angles, ϕ, where $0^o \leq \phi < 360^o$, in steps of 22.5^o.

5. Data for a single flapping flipper is taken by first moving the fore flipper out of the main flow, near the flume walls, and then flapping only the hind foil, at the same flapping frequency and amplitude, for 100 flaps again. This is repeated twice, centring the flipper between each run.

Due to the massive contribution to the raw data occurring from the inertial forces of the flapping apparatus, three more runs needed tom be carried out by flapping both flippers in phase while the flume tank is both off and empty. The flippers are again flapped 100 times, at the same l, f, s, and U_∞, and data is acquired for this motion.

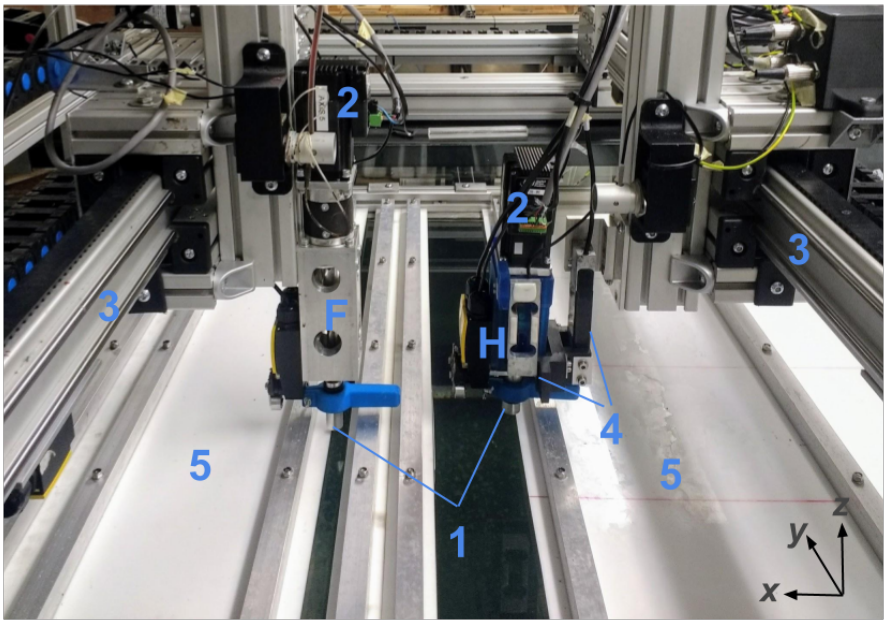

Figure 3.1: View from top of flume-tank showing the apparatus used to heave and pitch the flippers.

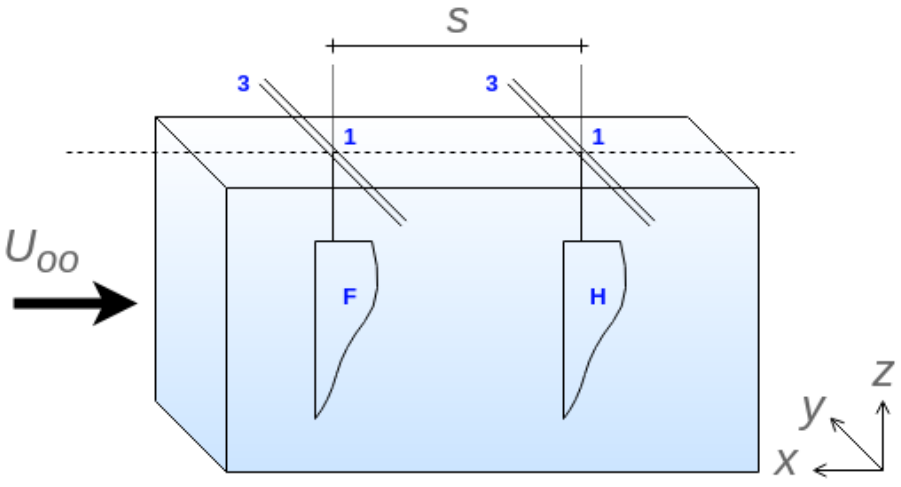

Figure 3.2: Rudimentary diagram of the placement of flippers within the flume tank. U_∞ is the flow velocity and s is the flipper spacing.

3.3 Cases to Run

In the main experiment, a full single case was first carried out using Luke Muscutt's fully rigid, $AR = 4$ (R4), flippers. Processing the data from this case, the values of ϕ for which the maximum and minimum C_T occur were obtained. Cases were then run for each flexible flipper, but only at those minimum/maximum C_T phase angles of the R4 flipper.

The full singular case was carried out for the flexible flipper(s) with the most promising minimum/maximum C_T values, for the same controlled variables as the fully rigid flipper case, as well as for greater values of l and f, to observe the effects of greater flipper deflections.

Tab. 3.1 summarises the cases carried out.

Case	Fore Flipper	Hind Flipper	Phases	AR	L	f	U_∞	s	St
1	Rigid	Rigid	All	4	0.05	$0.\dot{6}$	0.166	4c	0.4016
2	Rigid	Flexible	Max/Min C_T Phases	4	0.05	$0.\dot{6}$	0.166	4c	0.4016
3	Rigid	Flexible	All	4	0.05	$0.\dot{6}$	0.166	4c	0.4016
4	Rigid	Flexible	All	4	0.10	0.4	0.200	4c	0.4000

Table 3.1: The cases that were carried out on the flume tank, and the values of the controlled variables for each case.

For the flexible flipper runs, one more variable was kept constant, that variable being the flow impinging on the hind flipper. This is accomplished by only changing the flexibility of the hind flipper, and keeping the fore flipper fully rigid, allowing for a more direct comparison between the thrust augmentation of the fully rigid flipper and flexible flippers.

Case 4 was an extra case designed to observe the effects of greater flipper deflections, at similar St, and will be discussed in the following sections.

3.4 Data Acquisition & Processing

Two LabView projects had to be created by Dr. Muscutt, to allow for changing the flapping frequency during case 4, each with their own data acquisition frequency, due to the different scan engine times each project operated with.

Cases 1 - 3 used a scan engine time of 3ms, giving an acquisition frequency of $333.\dot{3}$ Hz. This means that for 1 flipper flapping cycle, there would be $(333.\dot{3}/f) = (333.\dot{3}/(2/3)) = 500$ data points, and so 50,000 data points for 100 flapping cycles.

Case 4 used a scan engine time of 2ms, and thus had a greater data acquisition frequency of 500 Hz, giving $(500/0.4) \times 100 = 125{,}000$ data points.

2000 data points were taken for each initial zero, for all cases.

Once the data had been aquired, it was transferred from the cRIO and converted to an excel spread-

sheet, allowing the data to be imported into a Matlab workspace for manipulation.

Dr. Muscutt's data processing code required there to be 2 sets of initial zero data and single flipper data for each case, which were averaged before being used for processing the main data (from each of the phases).

Once the necessary data had been imported, the processing began by setting the necessary constant variables (f, l, U_∞, data acquisition frequency, etc.).

1. The phase data and single flipper data (containing 100 flapping cycles each) are first zeroed by subtracting the averaged initial zero data.

2. A Butterworth filter is then applied to this zeroed data, to filter out the noisy data points, with a Ripple, $R_p = 1$, and and attenuation level $R_s = 40$

3. This filtered data can now be phase averaged to give the average flapping cycle, before the inertial data can be subtracted from it.

The inertial data undergoes the same process, and thus requires its own initial zeroes and single foil data, before it can be applied to the main phase data.

Once this has been carried out, the data with the inertial forces subtracted can finally be converted into forces (F_x & F_y) and moments (M), in the reference frame shown in Figs. 3.1 and 3.2.

From this force data, C_T can be found for each phase and single flipper case.

Figs. 3.3 & 3.4 illustrate these steps.

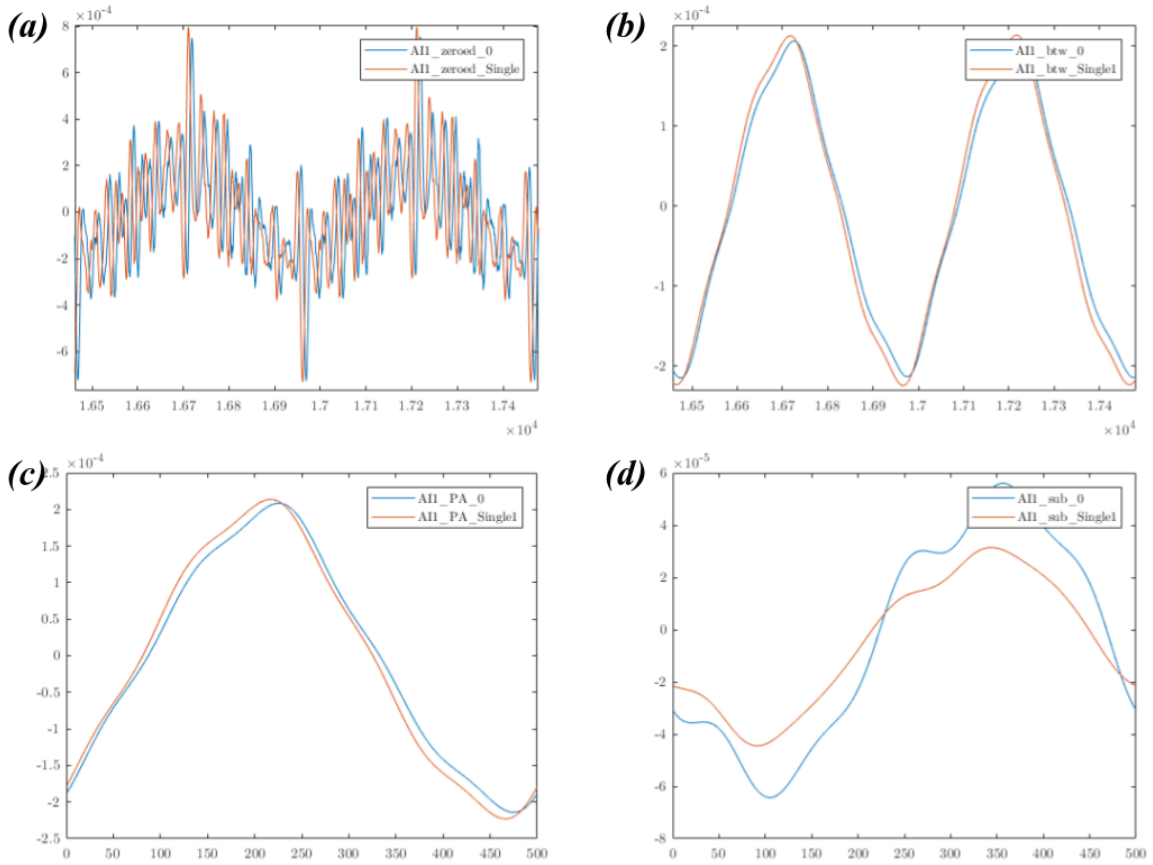

Figure 3.3: Plots of the data for the fully rigid (R4) flipper illustrating how the data for phase = 0^o and the single flipper data change as the data is processed. ***(a)*** *The raw data has been zeroed.* ***(b)*** *The zeroed data has been filtered.* ***(c)*** *The phase averaged, filtered data.* ***(d)*** *The zeroed, filtered and phase averaged inertial data has been subtracted from the main data.*

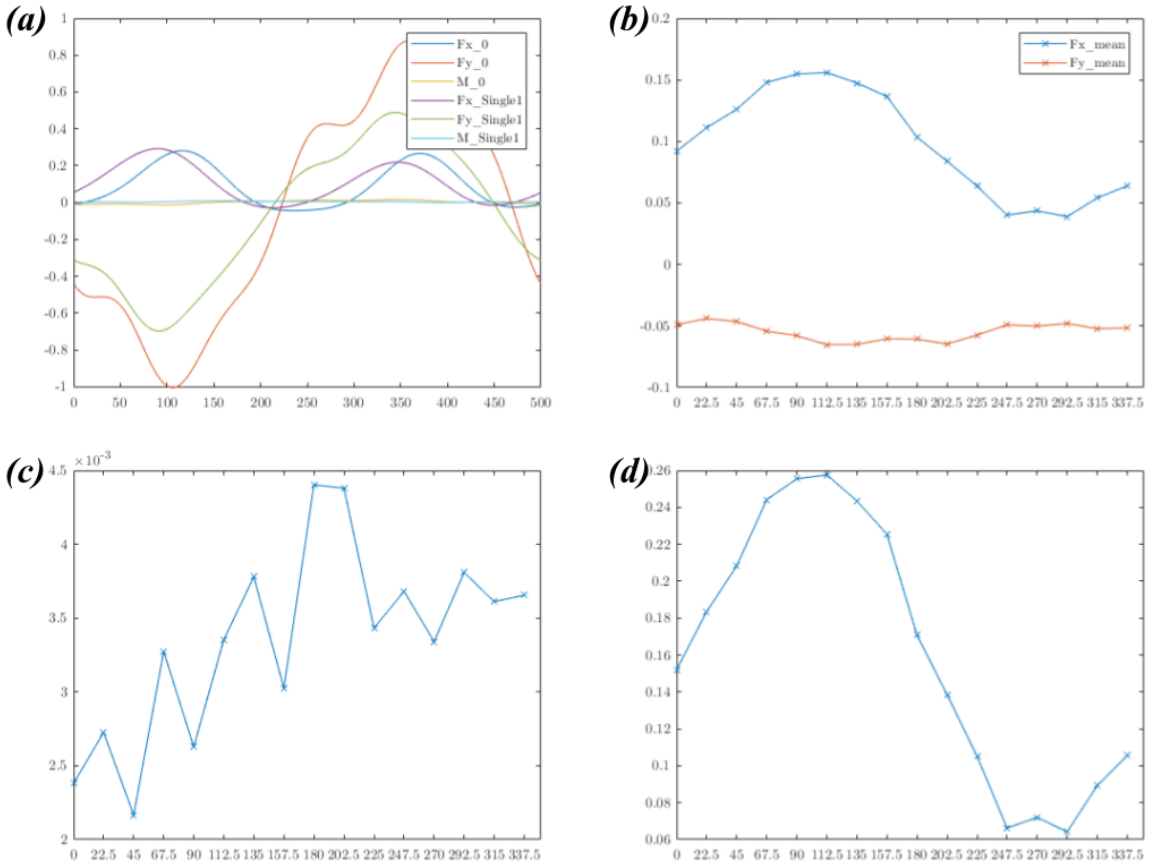

Figure 3.4: Plots of the data for the fully rigid (R4) flipper illustrating how the partly processed data for phase = 0^o and the single flipper are finally converted to forces, moments, and thrust coefficient. ***(a)*** *The data with inertial forces subtracted, from Fig. 3.3, (c), is converted into instantaneous forces and moments for one phase averaged flapping cycle.* ***(b)*** *&* ***(c)*** *The mean instantaneous forces and moments for one flapping cycle are calculated for each phase and plotted against phase.* ***(d)*** *C_T is calculated by dividing $F_{x,mean}$ by $\frac{1}{2}\rho U_\infty^2 A$, where A is the flipper's reference area.*

4

Results

4.1 Case 1

Tab. 4.1 shows the C_T data obtained for all phases investigated, and for the single flipper case, for the fully rigid AR4S flipper. C_T is normalised with $C_{T,R4,Single}$ (Coefficient of thrust for a single R4 flipper) for comparison. This will be done for all C_T obtained for all flipper flexibilities.

Phase [deg.]	C_T	$C_T/C_{T,R4,Single}$
0.0	0.15200	0.876285
22.5	0.18351	1.057951
45.0	0.20822	1.200394
67.5	0.24418	1.407694
90.0	0.25547	1.472822
112.5	0.25760	1.485077
135.0	0.24349	1.403715
157.5	0.22544	1.299664
180.0	0.17083	0.984824
202.5	0.13863	0.799198
225.0	0.10515	0.606205
247.5	0.06626	0.382014
270.0	0.07207	0.415469
292.5	0.06420	0.370120
315.0	0.08922	0.514388
337.5	0.10549	0.608160
Single Flipper	0.17346	1.000000

Table 4.1: Coefficient of thrust for the fully rigid, tandem, R4 flippers, for $0 \leq \phi < 360$, as well as for a single fully rigid flipper (highlighted).

$(EI)^*_{norm}$	$\phi = 112.5^o$		$\phi = 292.5^o$		**Single Flipper**	
	C_T	$C_T/C_{T,R4,Single}$	C_T	$C_T/C_{T,R4,Single}$	C_T	$C_T/C_{T,R4,Single}$
0.498	0.23339	1.345503	0.06556	0.377974	0.15316	0.882960
0.514	0.29706	1.712558	0.07662	0.441691	0.18610	1.072902
0.555	0.24971	1.439593	0.05902	0.340225	0.15944	0.919171
1.000	0.25760	1.485077	0.06420	0.370120	0.17346	1.000000
2.546	0.24135	1.391422	0.04819	0.277807	0.16485	0.950363

Table 4.2: Data produced for case 2, where the flippers were flapped at the maximum and minimum C_T phases from case 1.

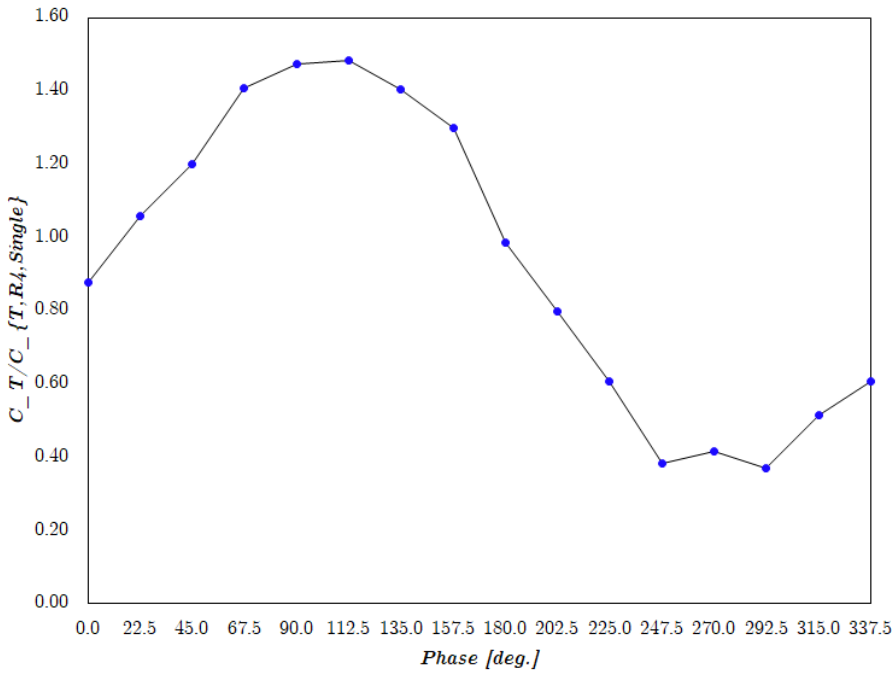

Figure 4.1: Plot of $C_T/C_{T,R4,Single}$ vs. Phase for the R4 Flipper

4.2 Case 2

Fig. 4.1 shows that the maximum and minimum C_T for the R4 flipper occur at $\phi = 112.5^o$ and $\phi = 292.5^o$, respectively. Thus, these were the phases chosen to be investigated for each flipper flexibility during this case.

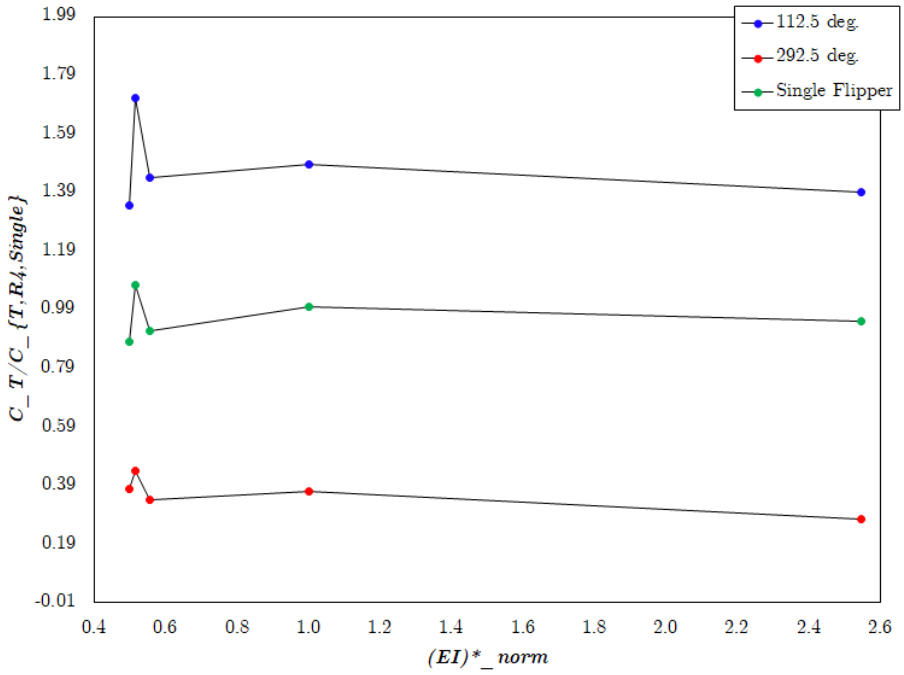

Figure 4.2: Plot of $C_T/C_{T,R4,Single}$ vs. $(EI)^*_{norm}$ for the flippers at $\phi = 112.5^o$, $\phi = 292.5^o$, and at their single flipper cases.

4.3 Case 3

From Fig. 4.2, it can be seen that the R1 and R2 flippers each have the lowest and highest C_T at $\phi = 112.5^o$, so full cases (flapping the flippers at all phases) were carried out for these two flippers. The data is tabulated in Tab. 4.3, and superimposed on one plot in Fig. 4.3, along with the data from case 1.

Phase [deg.]	**R1**		**R2**	
	C_T	$C_T/C_{T,R4,Single}$	C_T	$C_T/C_{T,R4,Single}$
0.0	0.03472	0.200192	0.13959	0.804765
22.5	0.08249	0.475557	0.16734	0.964718
45.0	0.11451	0.660162	0.20176	1.163175
67.5	0.14094	0.812522	0.21640	1.247539
90.0	0.16288	0.938999	0.17030	0.981799
112.5	0.16197	0.933778	0.25639	1.478141
135.0	0.16412	0.946180	0.24991	1.440755
157.5	0.15248	0.879043	0.21455	1.236905
180.0	0.11176	0.644288	0.18112	1.044162
202.5	0.06866	0.395824	0.12904	0.743917
225.0	0.02829	0.163072	0.08900	0.513088
247.5	-0.00096	-0.005516	0.06465	0.372730
270.0	0.01563	0.090133	0.07348	0.423632
292.5	0.00543	0.031276	0.06591	0.379998
315.0	0.01681	0.096903	0.08521	0.491240
337.5	0.05414	0.312098	0.12937	0.745828

Table 4.3: Coefficient of thrust for the R1 and R2 flippers, for $0 \leq \phi < 360$.

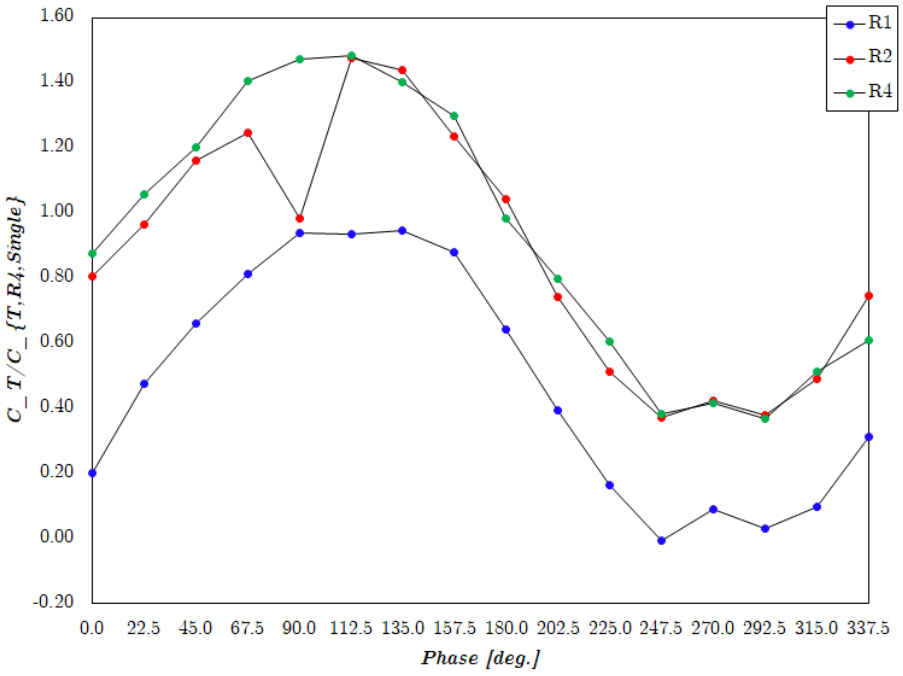

Figure 4.3: Plots of $C_T/C_{T,R4,Single}$ *vs.* ϕ *for flippers R1, R2 and R4.*

4.4 Case 4

Flippers R1 and R2 were tested at all phases once again, but this time at $l = 0.1m$, $f = 0.4Hz$ and $U_\infty = 0.2ms^{-1}$, so that they would undergo greater deflections that could be observed, and their effect quantified.

The R4 flipper was not investigated in this case however, due to time constraints. The C_T values have still been normalised with the same $C_{T,R4,Single}$ from case 1 to again understand how greater flipper deflections affect C_T.

Phase [deg.]	**R1**		**R2**	
	C_T	$C_T/C_{T,R4,Single}$	C_T	$C_T/C_{T,R4,Single}$
0.0	0.14817	0.854233	0.14761	0.850962
22.5	0.14642	0.844143	0.15176	0.874896
45.0	0.12244	0.705862	0.13884	0.800402
67.5	0.11376	0.655818	0.10885	0.627511
90.0	0.07405	0.426879	0.08142	0.469414
112.5	0.07338	0.423023	0.06505	0.375039
135.0	0.06351	0.366146	0.08227	0.474299
157.5	0.07947	0.458129	0.08358	0.481828
180.0	0.09734	0.561165	0.10459	0.602947
202.5	0.11729	0.676161	0.11915	0.686937
225.0	0.14216	0.819573	0.14113	0.813604
247.5	0.14911	0.859636	0.15556	0.896827
270.0	0.15974	0.920931	0.16474	0.949750
292.5	0.16615	0.957874	0.13113	0.756005
315.0	0.17668	1.018549	0.16873	0.972721
337.5	0.16631	0.958786	0.16712	0.963443

Table 4.4: Coefficient of thrust for the R1 and R2 flippers, for $0 \leq \phi < 360$, *when* $f = 0.4Hz$, $l = 0.1m$ *and* $U_\infty = 0.2ms^{-1}$.

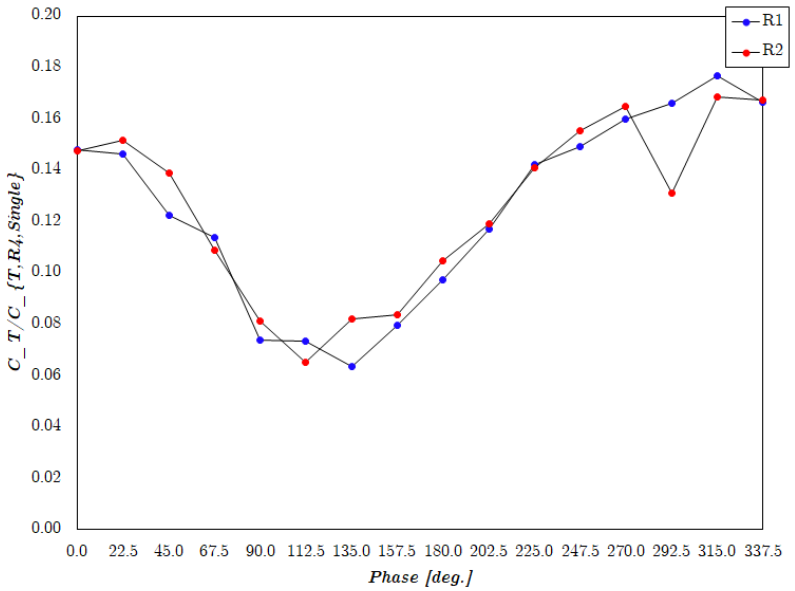

Figure 4.4: Plots of $C_T/C_{T,R4,Single}$ *vs.* ϕ *for flippers R1, R2, when* $f = 0.4Hz$, $l = 0.1m$ *and* $U_\infty = 0.2ms^{-1}$.

5

Analysis

Starting with case 1, the plot produced in Fig. 4.1 for the R4 flipper has a trend that conforms to those produced in Dr. Muscutt's work, and thus seems to be reliable. The same can be said of the of the ratio $C_T/C_{T,R4,Single}$ for this flipper, wih this tandem configuration producing a roughly 50% augmentation in thrust from the single flipper, similar to the 60% thrust augmentation reported in Muscutt, Dyke, et al. (2017b), at the maximum C_T phase angle.

As made clear in Section 1.2, flexible wings generally perform better than their rigid counterparts, and this is definitely seen in Fig. 4.2 where the hind flipper was exchanged for a flexible one, and the flippers flapped at the maximum and minimum C_T phases of the R4 flipper (case 2). Up to 70% thrust increases are seen when the hind flipper is made flexible (flipper R2), with the worst flexibility in this flow regime (R1) producing 25% more thrust than the single R4 flipper.

More interesting is the trend seen in this plot. There is certainly an optimum flexibility that can maximise C_T, and for this flow regime, it is the R2 flipper. Increasing or decreasing flexibility from this optimum sees relatively dramatic decreases in C_T, especially at the maximum C_T phase angle. This is true for both the single and tandem flipper configurations.

Further, it is clear that even if these flippers have high spanwise rigidity, but still some chordwise rigidity, like the high $(EI)^*$ R5 flipper, there will be no thrust augmentation. This suggests that spanwise flexibility takes precedence over chordwise flexibility when trying to extract noticeable thrust augmentations from these flexible flippers.

One discrepancy that can be observed in this data are the points corresponding to the R3 flipper. For the maximum and minimum C_T phase angles, as well as for the single flipper cases, this flipper performed poorly even when compared to the more rigid R5 and R4 flippers.

Due to their interesting performance in case 2, flippers R1 and R2 were chosen for further investigation in case 3. This was done to observe any changes in the optimum phase angles that may have caused the R1 flipper, the most flexible flipper investigated, to perform comparatively poorly.

Indeed, there are no grand changes in the optimum phase angles. The optimum phase angle for the R1 flipper does occur at a slightly different phase of 135^o.

What is intriguing is how, in this case, the R2 flipper performs almost exactly the same as the R4 flipper, contrasted to the +20% thrust augmentation this flipper over the fully rigid R4 flipper in case 2. In fact, this case was repeated to investigate this, with no change, suggesting that the

results for this flipper in case 2 may have been anomalous. There were, however, a few days before case 3 could be carried out, so damage or fatigue to the load cells may have caused this anomaly.

Flippers R1 and R2 were once again investigated at all phases, but with different flapping frequency, amplitude and flow velocity. Again, both flippers produce thrust augmentation (roughly 17%), but not with the same magnitude as in cases 1, 2 and 3, and there is no noticeable difference between the results for each flexibility. Clearly, greater flipper deflections are less desirable when looking for greater thrust augmentations.

However, at the minimum C_T phase angle, the detrimental thrust augmentation (40% for this case) is much less than that during the previous cases, reaching a maximum of roughly 60% (Fig. 4.2) and 100% (Fig. 4.3. This may however be a feature resulting from the greater flow velocity.

With this insight, it seems that flippers that can undergo greater deflections may be more suitable when flapping at lower frequencies (which may correspond to slower swimming speeds).

As has already been noticed, there are glaring discrepancies between the results of these cases, the most notable being that the R3 flipper performing up to 10% worse (Fig. 4.2) than more rigid flippers which had more than double the $(EI)^*$ value. This may have arisen from faults in the manufacture of this flipper, the attachment rod not being properly secured in the flipper or the flapping apparatus for example. Another source of human error would be poor centering of the flippers with respect to the apparatus (before they could be centered by the cRIO). The cRIO would also occassionally fail to center the pitch of the hind foil, meaning the pitch of the hind foil would have to be centred by eye.

As seen in Fig. 3.3 (d), subtracting the inertial data from the phase averaged data during post-processing led to misshapen sinusoidal trends in the phase-averaged data. This may have been incorporated into the final calculations of forces, and thus coefficient of thrust, causing the increased occurrence of anomalous data points seen in Figs. 4.3 & 4.4, at $\phi = 90^o$ and $\phi = 292.5^o$ respectively.

6

Conclusion

FLexible flippers in a tandem wing configuration have been given a preliminary investigation in this report, and have shown to produce notable thrust augmentations of up to 70% more than a single rigid flipper. This result makes flexible flippers seem a promising candidate for use on the Project Atlantis UUV.

A rudimentary non-dimensional number was used to define spanwise flipper flexibility, $(EI)^*$. Results in Fig. 4.2 showed that in the range $0.4 \leq (EI)^* \leq 0.6$, there is an optimum flexibility that produces a maximum thrust augmentation. Clearly, this range of $(EI)^*$ requires more detailed analysis.

There are however various inconsistencies between the cases investigated and these need to be addressed through more rigorous research so that more reliable data can be produced.

References

Barannyk, Oleksandr, Bradley J Buckham, and Peter Oshkai (2012). "On performance of an oscillating plate underwater propulsion system with variable chordwise flexibility at different depths of submergence". In: *Journal of Fluids and Structures* 28, pp. 152–166.

Carpenter, Kenneth et al. (2010). "Plesiosaur swimming as interpreted from skeletal analysis and experimental results". In: *Transactions of the Kansas Academy of Science* 113.1/2, pp. 1–34.

Epps, Brenden P et al. (2016). "On the inter-foil spacing and phase lag of tandem flapping foil propulsors". In: *Journal of Ship Production and Design.* Pp. 1–39.

Formlabs (n.d.). *Flexible Datasheet*. URL: https://formlabs.com/media/upload/Flexible-DataSheet.pdf.

Frey, E and J Riess (1982). "Considerations concerning plesiosaur locomotion". In: *Neues Jahrbuch für Geologie und Paläontologie, Abhandlungen* 164, pp. 193–194.

Gent, Alan N (1958). "On the relation between indentation hardness and Young's modulus". In: *Rubber Chemistry and Technology* 31.4, pp. 896–906.

Heathcote, Sam, Z Wang, and Ismet Gursul (2008). "Effect of spanwise flexibility on flapping wing propulsion". In: *Journal of Fluids and Structures* 24.2, pp. 183–199.

Innofil3D (n.d.). *Technical Data Sheet Innofil3D PRO1*. URL: https://www.innofil3d.com/material-data/professional-technical-data/.

Katz, J and D Weihs (1978). "Hydrodynamic propulsion by large amplitude oscillation of an airfoil with chordwise flexibility". In: *Journal of Fluid Mechanics* 88.3, pp. 485–497.

Larkin, Nigel, Sonia O'Connor, and Dennis Parsons (2010). "The virtual and physical preparation of the Collard Plesiosaur from Bridgwater Bay, Somerset, UK". In: *Geological curator* 9.3, p–107.

Liu, Shiqiu et al. (2015). "Computer simulations imply forelimb-dominated underwater flight in plesiosaurs". In: *PLoS computational biology* 11.12, e1004605.

Ltd., Perspex Distribution (n.d.). *Perspex Cast Acrylic Data Sheet*. URL: https://www.plasticonline.co.uk/media/wysiwyg/pdf-downloads/Technical/Perspex_Cast_Acrylic_Data_Sheet.pdf.

Muscutt, Luke (2017). "The Hydrodynamics of Plesiosaurs". PhD thesis. University of Southampton - Faculty of Engineering and the Environment.

Muscutt, Luke, Gareth Dyke, et al. (2017b). "The four-flipper swimming method of plesiosaurs enabled efficient and effective locomotion". In: *Proc. R. Soc. B*. Vol. 284. 1861. The Royal Society, p. 20170951.

Muscutt, Luke, Gabriel Weymouth, and Bharathram Ganapathisubramani (2017a). "Performance augmentation mechanism of in-line tandem flapping foils". In: *Journal of Fluid Mechanics* 827, pp. 484–505.

Newman, B and LB HALSTEAD Tarlo (1967). "A giant marine reptile from Bedfordshire". In: *Animals* 10.2, pp. 61–63.

Online, Plastic (n.d.). *FAQ*. URL: https://plasticonline.co.uk/faqs.

Shusheng, Bi and Cai Yueri (2012). "Effect of spanwise flexibility on propulsion performance of a flapping hydrofoil at low Reynolds number". In: *Chinese Journal of Mechanical Engineering* 25.1, pp. 12–19.

Taylor, Graham K, Robert L Nudds, and Adrian LR Thomas (2003). "Flying and swimming animals cruise at a Strouhal number tuned for high power efficiency". In: *Nature* 425.6959, pp. 707–711.

Toolbox, The Engineering (n.d.). *Young's Modulus - Tensile and Yield Strength for common Materials*. URL: https://www.engineeringtoolbox.com/young-modulus-d_417.html.

Usherwood, James R and Fritz-Olaf Lehmann (2008). "Phasing of dragonfly wings can improve aerodynamic efficiency by removing swirl". In: *Journal of The Royal Society Interface* 5.28, pp. 1303–1307.

Weymouth, Gabriel D and Dick KP Yue (2011). "Boundary data immersion method for Cartesian-grid simulations of fluid-body interaction problems". In: *Journal of Computational Physics* 230.16, pp. 6233–6247.

Wu, P et al. (2011). "Structural dynamics and aerodynamics measurements of biologically inspired flexible flapping wings". In: *Bioinspiration & biomimetics* 6.1, p. 016009.

Young, John et al. (2009). "Details of insect wing design and deformation enhance aerodynamic function and flight efficiency". In: *Science* 325.5947, pp. 1549–1552.

A

Calculating *EI*

```
import numpy as np
import matplotlib.pyplot as py


### Mass from solidworks
m_sw = np.array([72.83, 78.53, 78.08, 98.71, 86.27]) * (1 / 1000)


### Young's Modulus & Volume of each component
# volume is found using solidworks
# _ar = Attachment rod
# _perspex = perspex endoskeleton
# _steel = steel endoskeleton
# _flipper = flipper with cut-outs for endoskeleton and attachment rod
# _flippersolid = flipper with cut-out for attachment rod only
# _fl = whole flipper assembly
# _innofil = Dr. Muscutt's fully rigid AR4S flipper

E_ar = 180. * (10 ** (9))
V_ar = 981.75/1000000000

E_perspex = 3210. * (10 ** (6))
V_perspex = 4596.67/1000000000

E_steel = 206. * (10 ** (9))
V_steel = 3083.33/1000000000

E_rubber = 9.351374951 * (10 ** (6))

E_innofil = 2635.5 * (10 ** (6))

V_flipper = 57619.86/1000000000
V_flippersolid = 62685.68/1000000000

V_fl = 63667.43/1000000000


### E_eff
# _1 = foam endoskeleton
# _2 = solid rubber flipper
# _3 = perspex endoskeleton
# _4 = steel endoskeleton
E_eff_1 = (E_ar * (V_ar/V_fl)) + (E_rubber * (V_flipper/V_fl))
E_eff_2 = (E_ar * (V_ar/V_fl)) + (E_rubber * (V_flippersolid/V_fl))
E_eff_3 = (E_ar * (V_ar/V_fl)) + (E_rubber * (V_flipper/V_fl)) + (
        E_perspex * (V_perspex/V_fl))
E_eff_4 = (E_ar * (V_ar/V_fl)) + (E_rubber * (V_flipper/V_fl)) + (
        E_steel * (V_steel/V_fl))
E_eff_5 = (E_ar * (V_ar/V_fl)) + (E_innofil * (V_flippersolid/V_fl))


### Moment of Inertia from Solidworks about pitch axis, converted to SI units,
#   and normalized with the total flipper mass
I_sw_1 = (1/1000000000.) * np.matrix([[496916.02, -2.07, 75748.33],
                                      [-2.07, 524680.05, -2.48],
                                      [75748.33, -2.48, 28834.68]])

```

```
I_sw_2 = (1/1000000000.) * np.matrix([[552967.11, -2.07, 79127.76],
                                      [-2.07, 581049.21, -2.48],
                                      [79127.76, -2.48, 29161.01]])

I_sw_3 = (1/1000000000.) * np.matrix([[547820.32, -2.07, 79053.83],
                                      [-2.07, 575906.46, -2.48],
                                      [79053.83, -2.48, 29164.47]])

I_sw_4 = (1/1000000000.) * np.matrix([[751253.51, -2.07, 92120.78],
                                      [-2.07, 780613.75, -2.48],
                                      [92120.78, -2.48, 30447.76]])

I_sw_5 = (1/1000000000.) * np.matrix([[612826.44, -2.30, 87796.97],
                                      [-2.30, 643985.20, -2.75],
                                      [87796.97, -2.75, 32353.17]])


### Calculating EI
EI1 = I_sw_1 * E_eff_1
EI2 = I_sw_2 * E_eff_2
EI3 = I_sw_3 * E_eff_3
EI4 = I_sw_4 * E_eff_4
EI5 = I_sw_5 * E_eff_5

EI_1 = I_sw_1 * (1 / m_sw[0]) * E_eff_1
EI_2 = I_sw_2 * (1 / m_sw[1]) * E_eff_2
EI_3 = I_sw_3 * (1 / m_sw[2]) * E_eff_3
EI_4 = I_sw_4 * (1 / m_sw[3]) * E_eff_4
EI_5 = I_sw_5 * (1 / m_sw[4]) * E_eff_5

EIxx = np.array([EI1.item((0,0)), EI2.item((0,0)), EI3.item((0,0)),
        EI4.item((0,0)), EI5.item((0,0))])
EI_xx = np.array([EI_1.item((0,0)), EI_2.item((0,0)), EI_3.item((0,0)),
        EI_4.item((0,0)), EI_5.item((0,0))])
EI_yy = np.array([EI_1.item((1,1)), EI_2.item((1,1)), EI_3.item((1,1)),
        EI_4.item((1,1)), EI_5.item((1,1))])
EI_zz = np.array([EI_1.item((0,0)), EI_2.item((2,2)), EI_3.item((2,2)),
        EI_4.item((2,2)), EI_5.item((2,2))])


### Normalizing EI with Dynamic Pressure
# For Cases 1 - 3, where U_infinity = 0.166 m/s
nodim = 1 / (0.5 * 997.6 * (0.166 ** 2) * (0.1 ** 2))

EI_xx_ndim = EI_xx * nodim
EI_yy_ndim = EI_yy * nodim
EI_zz_ndim = EI_zz * nodim

# For Case 4, where U_infinity = 0.2 m/s
nodim2 = 1 / (0.5 * 997.6 * (0.2 ** 2) * (0.2 ** 2))

EI_xx_ndim_2 = EI_xx * nodim2
EI_yy_ndim_2 = EI_yy * nodim2
EI_zz_ndim_2 = EI_zz * nodim2

print('EIxx = ',EIxx)

print('EI_xx_ndim = ',EI_xx_ndim)

print('EI_xx_ndim_2 = ',EI_xx_ndim_2)
```